Materials Characterization 228 (2025) 115372

Contents lists available at ScienceDirect

Materials Characterization

journal homepage: www.elsevier.com/locate/matchar

Microstructure and tensile properties of TIB_2-reinforced Al-2618 thin walls produced by laser powder bed fusion

G. Lupi [a], L. Mariotti [a], A. Mistrini [a], J. Larsson [b], L. Patriarca [a,*], R. Casati [a,*]

[a] Department of Mechanical Engineering, Politecnico di Milano, Via G. La Masa 34, 20156 Milano, MI, Italy
[b] European Space Agency, Keplerlaan 1, 2201 AZ Noordwijk, The Netherlands

ARTICLE INFO

Keywords:
Additive manufacturing
Laser powder bed fusion
Metal matrix composites
Aluminium alloys
Powder functionalization

ABSTRACT

This study focuses on enhancing the processability and mechanical properties of the Al-2618 Al alloy by functionalizing powder with TiB_2. Four different methods have been used to add TiB_2 particles to the Al alloy powder: i) low-pressure plasma, ii) low-energy and iii) high-energy mechanical mixing, and iv) pre-alloying by gas-atomization. Comprehensive characterization of composite powders was conducted, followed by Laser Powder Bed Fusion (LPBF) manufacturing of samples. High-density printed composites were achieved with all powder feedstocks, with homogeneous dispersion of TiB_2 and absence of cracks. Borides effectively promoted heterogeneous nucleation of α-Al phase, suppressing epitaxial growth and leading to a fine equiaxed microstructure. Upon preliminary study on different heat-treatment routes (T6 and T5), tensile tests aided by Digital Image Correlation (DIC) have been performed to assess the mechanical properties. Results show significant enhancements in yield and ultimate strengths post-heat treatments. Despite lower ductility, pre-alloyed powder exhibited superior mechanical performance due to nano-metric TiB_2 formation.

1. Introduction

The application of Additive Manufacturing (AM) is rapidly expanding, enabling the design of complex part geometries that are unattainable with traditional technologies. AM technologies can also facilitate the adoption of novel functional materials, allowing for the achievement of specific performance requirements [1–3]. This family of technologies has exponentially grown during recent years, with techniques such as Laser Powder Bed Fusion (LPBF) and Directed Energy Deposition being widely used in several industrial sectors [4,5]. However, the alloys currently in use have been developed for the traditional manufacturing processes. Consequently, a key challenge is the development of tailored alloys to further advance the adoption of AM technologies. The processability of certain nickel and aluminium alloys is difficult due to their susceptibility to solidification and liquation cracking, whereas that of copper is poor due to high laser-reflectivity, leading to the request of novel material grades [6–9]. Materials with improved combinations of physical and mechanical properties for demanding applications can be obtained by ad-hoc compositions or by adding micro- or nano-sized ceramic nanoparticles to create Metal Matrix Composites (MMC) [10–12].

Ceramic reinforcements are generally added to enhance the mechanical properties of the matrix material, including stiffness and strength [13–15]. Moreover, thanks to their high thermodynamic stability, they are particularly suitable for high-temperature applications. MMC can be obtained by mixing ceramic particles with metal powder or directly by gas atomization, i.e. by promoting in-situ reaction to form fine ceramic particles in the crucible before the molten material is poured through the nozzle. However, in the latter case, the amount of ceramic phase must be limited to avoid nozzle clogging and sedimentation of the ceramic fraction [16,17]. An alternative way to manufacture MMC consists in promoting in-situ reactions during LPBF by mixing metal powder with additives that react in the melt pool to form ceramic reinforcement [18,19]. However, this strategy faces challenges, primarily due to the uneven dispersion of reactive particles within the metal powder. This leads to an inhomogeneous distribution of reinforcement particles and the presence of unwanted unreacted particles in the final printed MMC [20,21]. Another interesting approach is the modification of the surface of powder particles. Various techniques can be utilized to decorate powder particles with ceramic particles, including mechanical (blending, milling), chemical (Chemical Vapor Deposition, layer-by-layer methods), electro-chemical (electroless

* Corresponding authors.
E-mail addresses: luca.patriarca@polimi.it (L. Patriarca), riccardo.casati@polimi.it (R. Casati).

https://doi.org/10.1016/j.matchar.2025.115372
Received 13 February 2025; Received in revised form 4 June 2025; Accepted 9 July 2025
Available online 10 July 2025

Table 1
Nominal chemical composition of the Al-2618 powders and PGA alloy (wt%).

	Cu	Fe	Mg	Ni	Si	Ti	Zn	B	Cr	Mn	Al
Al-2618 (1)	2.3	1.2	1.6	1.0	0.2	0.06	0.02	–	<0.01	0.01	Balance
Al-2618 (2)	1.8	1.0	1.3	1.0	0.2	–	0.02	–	–	–	Balance
PGA	2.1	1.0	1.3	1.0	0.3	4.1	–	0.8	–	–	Balance

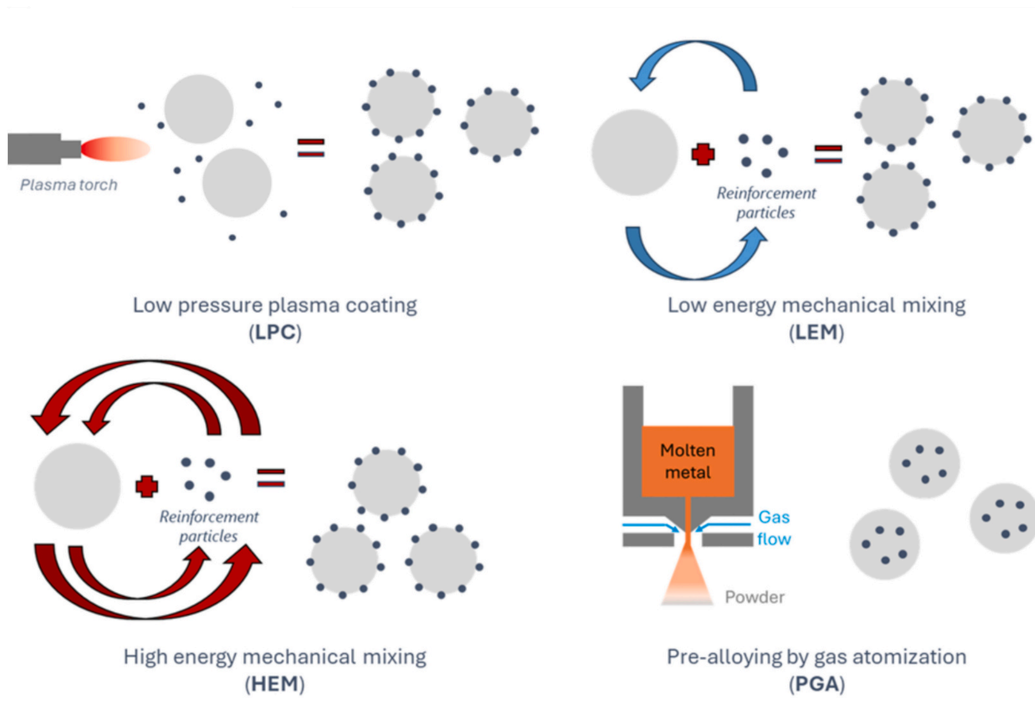

Fig. 1. Schematic representation of the four different methods used to obtain composite powder feedstocks.

deposition, electrolytic deposition, electrostatic self-assembly), and physical methods (plasma, Physical Vapor Deposition) [22–25].

This work aims to investigate different methods to produce Al-2618-TiB_2 MMC feedstocks. The Al-2618 is a widely used high-strength aluminium alloy for high temperature applications, and the addition of TiB_2 particles was proved to increase its mechanical properties [26], including the strength and the stiffness. However, Al-2618 has a high tendency to form hot cracks [27]. In this regard, TiB_2 was observed to be an effective grain refiner, capable of reducing the alloy's susceptibility to hot cracking [28]. Considering these main advantages of reinforcing the Al-2618 with TiB_2 particles, this study focuses on the development and characterization of the composite feedstock, and on the effect of the different powder configurations on the final material properties. Four different methods were used to produce composite powders: i) low and ii) high energy mechanical mixing, iii) plasma assisted coating and iv) pre-alloying by gas atomization. The goal of this work is to fabricate a MMC containing 7 wt% TiB_2, with enhanced LPBF processability. This relatively high ceramic content is expected to increase the elastic modulus and improve the overall mechanical strength of the material. Indeed, the target content of 7 wt% TiB_2 was selected based on a preliminary estimation aimed at achieving a substantial increase in the elastic modulus of the Al-2618 matrix. Using the rule of mixtures [29], an increase of approximately 20 % in elastic modulus is expected with this reinforcement level compared to the unreinforced alloy (from 72 GPa to 94 GPa). The different feedstock materials were then characterized to highlight the advantages and disadvantages of each production method. Initially, the powders were fully characterized by Field Emission Scanning Electron Microscope (FE-SEM) and mechanical sieve. Then, bulk samples were manufactured by LPBF using the four powder batches. FE-SEM and EBSD analyses were carried out to assess the microstructural features of the manufactured MMC. Micro-tensile tests were conducted on bulk materials that were heat-treated according to different schedules and designed with a geometry representative of a thin wall structure. Digital Image Correlation (DIC) technique was used to analyse the material deformation during tensile testing, providing insights into the heterogeneity of local deformation and its impact on the overall mechanical behaviour.

2. Experimental

2.1. Powder feedstocks

Three Al-2618/7wt.%TiB_2 powder feedstocks were obtained using different ex-situ processing routes, i.e.: i) low energy mechanical mixing (LEM), ii) high energy mechanical mixing (HEM), and iii) low-pressure plasma coating (LPC). Lastly, an Al-2618 powder pre-alloyed with Ti and B was obtained by gas atomization.

Two different Al-2618 powders were procured for the ex-situ composite powder feedstocks. These two powder feedstocks are referred to as Al-2618 (1) and Al-2618 (2) and their chemical compositions are reported in Table 1. Al-2618 (1) powder was supplied by Kymera International [30]. This powder shows D10, D50, and D90 equal to 29.0 μm, 48.6 μm and 78.8 μm, respectively. Al-2618 (2) was procured from IMR Metal Powder Technologies Gmbh [31]. It shows D10, D50, and D90 equal to 18.5 μm, 39.8 μm and 74.4 μm, respectively.

The LEM composite powder was mixed with a laboratory drums mixer (Adler Mixer-T0). The process was carried out for 8 h at 40 rpm under Ar. The Al-2618 (1) powder was mixed with TiB_2 particles with

Table 2
Process parameters used to print the samples.

Laser power	200 W
Time of exposure	140 µs
Point distance	100 µm
Hatch distance	80 µm
Layer thickness	25 µm

polygonal shape and average diameter of 4 µm supplied by Höganäs AB [32].

IMR Metal Powder Technologies Gmbh [31] produced the HEM composite feedstock by using a high-energy dry mixer. The process was conducted under nitrogen at room temperature. The mixer equipped with an internal cooling system helped to reduce the heat generated by particle friction. TiB_2 particles with average diameter of 2 µm (produced by Treibacher industrie AG [33]) were mixed with the Al-2618 (2) powder.

The same boride particles were employed in the production of LPC powder by AM4AM s.à.r.l using the Al-2618 (2) powder [34]. LPC process consists in injecting a mixture of metal powder and ceramic in a cold plasma discharge. The energy of the plasma activates the surface of both types of particles and induces the preferential attraction between them (smallest on largest). After this treatment, the unreacted ceramic/metal particles were removed, while the functionalized powder was collected.

The fourth powder feedstock, herein referred to PGA (i.e. pre-alloyed gas atomized powder), was produced by Kymera International [30] through gas atomization by pre-alloying the molten bath with Ti and B. The chemical composition is reported in Table 1. Al powder shows D10, D50, and D90 equal to 29.8 µm, 43.0 µm and 61.7 µm, respectively. This production method presents limitations, particularly regarding boron concentration. Boron tends to react with Ti and separate from the melt thus clogging the nozzle. The maximum content of titanium and boron that was achieved is Ti = 4.1 wt% B = 0.8 wt%, resulting in a total TiB_2 of 2.6 wt%.

The four processes resulted in four different functionalised powders considering TiB_2 interaction with matrix powder as shown in the schematic of Fig. 1. LPC, LEM and HEM processes determined the surface enrichment of Al particles (matrix powder) with TiB_2; on the other hand, the PGA process results in TiB_2 particles directly embedded in the matrix powders thus producing a MMC powder.

2.2. Processing

A Renishaw AM250 equipped with Reduced Built Volume (RBV) module was used to manufacture cubic samples (8x8x8 mm^3) for density and microstructural analyses of the bulk materials. Based on material density, the optimal combination of parameters that allows to achieve the highest density considering all the different powder feedstocks has been identified and reported in Table 2 (optimization procedure is not detailed in this manuscript). The printing parameters reported in Table 2 allowed to obtain samples with relative density higher than 99.2 % with all the powder feedstocks and the same combination of printing parameters were used to print cubes and specimens for tensile tests.

2.3. Material characterization

The investigation of powder morphology and distribution of the reinforcement particles was performed with a Field Emission Scanning Electron Microscope (FE-SEM) model Zeiss Sigma 500 equipped with energy dispersive X-ray analysis (EDX) and secondary electrons and backscattered electrons detectors (EBSD).

Bulk samples microstructures were analysed using a light optical microscope (LOM) and FE-SEM after their preparation with standard grinding and polishing procedures. Keller's reagent was employed in the chemical etching to reveal the microstructural features. Image analysis with ImageJ software was performed to assess the relative density of the samples. The density results were confirmed by Archimedes method measurements performed using an ME204 Mettler Toledo analytical balance in demineralized water at a controlled temperature of 20 °C.

The ex-situ mixed MMC powders were sieved after the powder functionalization process by means of a mechanical sieve with a 63 µm mesh. The effect of sieving on the different ex-situ mixed MMC powders (LPC, LEM, and HEM powder feedstocks) was investigated by FE-SEM analysis. For this purpose, powder samples were collected and inspected before and after the sieving process. Analysis of FE-SEM images (three per powder batch) was also performed by ImageJ software [35].

The study of the aging behaviour was carried out using 8 × 8 × 8 mm^3 cubes produced with the HEM powder feedstock. Two heat treatment cycles were investigated:

- T6 treatment: solution treatment (ST) at 530 °C for 1 h, followed by water quenching (WQ) and artificial aging at either 160 °C or 180 °C for 1, 2, 4, 8, or 24 h.
- T5 treatment (direct aging, DA): aging directly from as-built condition at 180 °C for 1, 2, 4, 8, or 24 h.

The effect of the heat-treatments was quantified through Vickers microhardness measurements, carried out using a Future-Tech FM-810 system. The samples were subjected to a load of 300 g_f for dwell time of 10 s. Age hardening curves were constructed for each temperature

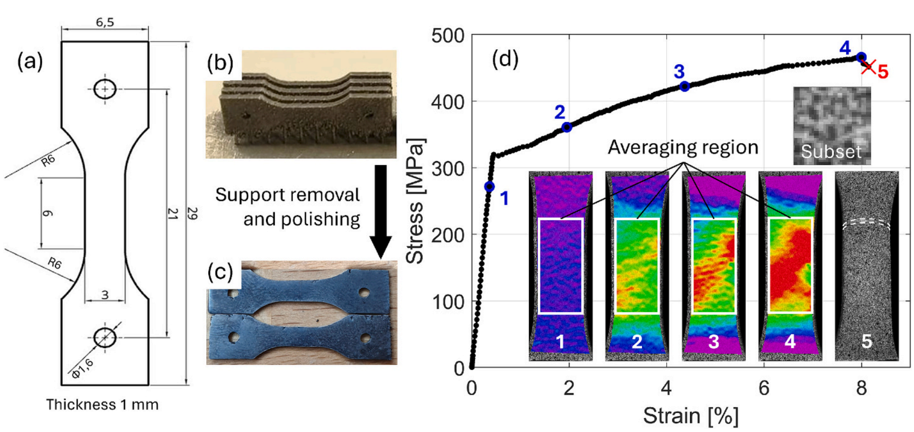

Fig. 2. a) Nominal dimensions of tensile specimen in mm, b) representative images of printed samples, c) representative images of samples after polishing and d) representative image of the DIC technique with an example of the subset for correlation and the stress-strain plot obtained by averaging the strain within the white box.

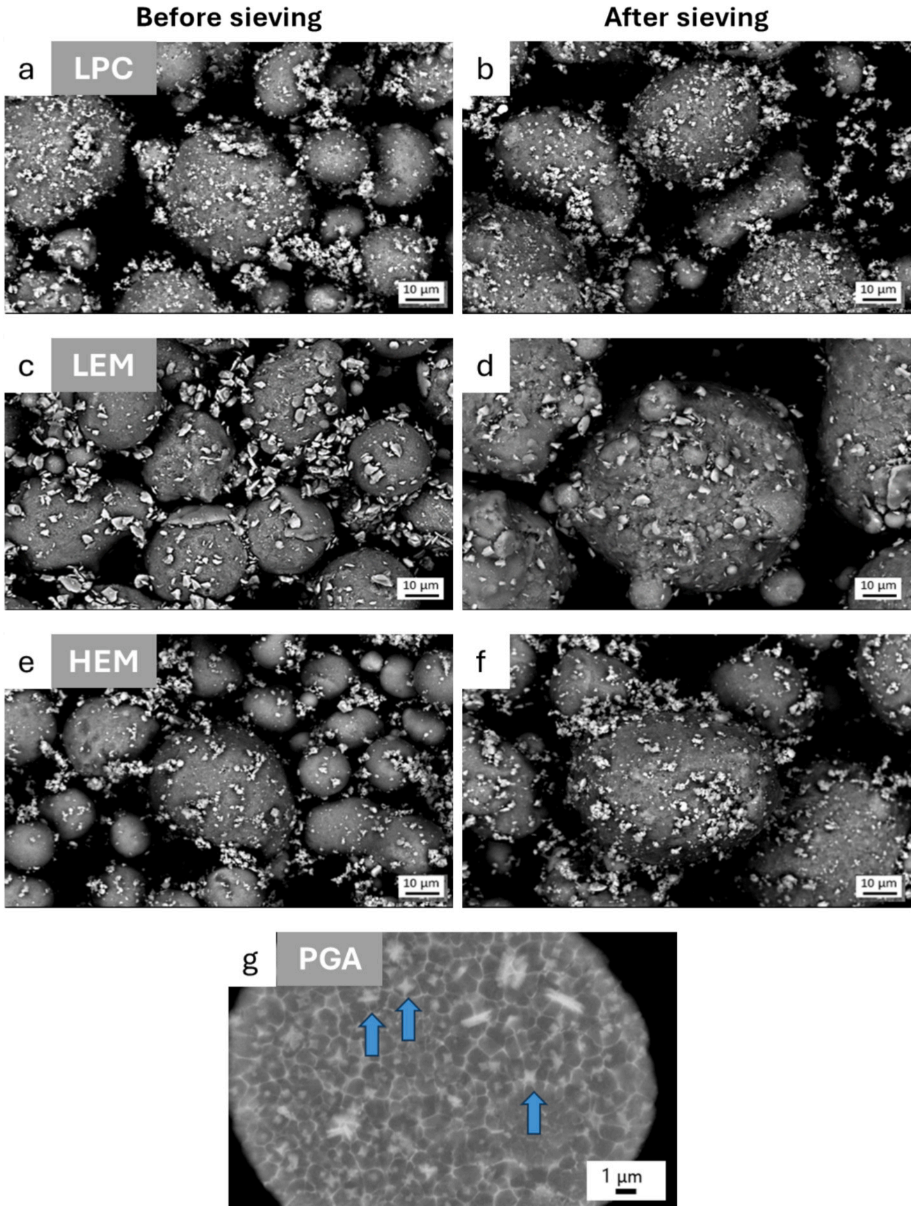

Fig. 3. FE-SEM images of the powder feedstocks produced by a), b) LPC, c), d) LEM, and e), f) HEM before and after sieving. g) PGA powder where blue arrows indicate TiB2 particles. (For interpretation of the references to colour in this figure legend, the reader is referred to the web version of this article.)

considering average values and standard deviations. Based on the results obtained, the optimal T6 and T5 tempers were selected and applied to the specimens later subjected to mechanical testing. The same heat-treatments route was applied to the other bulk samples produced with different powder feedstocks. The investigation of the microstructure was accomplished with FE-SEM analysis.

2.4. *Mechanical testing*

Micro-tensile tests were performed using a 5 kN Deben tensile machine with a displacement rate of 0.3 mm/min. The dog-bone geometry of the micro-tensile samples is specified in Fig. 2.a. The samples were directly manufactured in the final shape as show in Fig. 2.b. After printing, the samples underwent grinding and mechanical polishing. As shown in Fig. 2.c, defects were observed in the lower part of the specimens, near the base plate at the supports. As a result, some variability in mechanical performance is expected, particularly affecting the strain at failure and the ultimate tensile strength (UTS).

The strain calculation was conducted using a DIC technique. Samples were prepared for DIC by spraying firstly white paint, and successively black paint to generate a random speckle pattern. The paints were both deposited on the specimen surface using an Iwata CM-B airbrush equipped with a 0.18 mm nozzle diameter. The black spots resulted in an average diameter of approximately 30 $\pm$ 4 µm. The sample under testing was illuminated using blue light at 45° on the sample surface to maximize the speckle contrast. The images were captured every 500 ms during the test using a 2 Megapixel Allied Vision Manta CCD optical microscope equipped with a lens system produced by Optem. A field of view of approximately 6.58 $\times$ 8.68 mm has led the final pixel resolution to 5.3 µm/pixel.

VIC-2D software was employed to perform image correlation using a square subset of 37 pixels visible in Fig. 2.d and a step of 3 pixels. The axial DIC strains were then averaged on the rectangular area of 2.5 $\times$ 5 mm centred on the most strained zone as shown in Fig. 2.d. The process is clarified by showing an example of four strain maps (numbered from 1 to 4) that correspond to the highlighted data points on the stress-strain curve. The frame number 5 is displayed to highlight the fracture site.

A total of 24 tensile tests were performed. Specimens were tested in

Table 3
Concentrations of TiB_2 before and after sieving obtained by image analysis of FE-SEM pictures.

	LEM	LPC	HEM
Before sieving (TiB_2 (%))	7.6 ± 1.0	6.3 ± 0.5	6.0 ± 0.7
After sieving (TiB_2 (%))	2.7 ± 0.1	6.9 ± 0.8	6.8 ± 1.0

as-built (AB) conditions and in two heat-treated conditions, i.e. T5 (180 °C for 4 h) and T6 (530 °C for 1 h, WQ and 180 °C for 1 h). Two specimens for each condition were tested.

From the stress-strain curves, the elastic modulus was calculated by fitting the linear part between the 0.1·σy and the 0.8·σy using least-square method, where σ_y indicates the yield stress (YS). The ultimate tensile strength (UTS) was also recorded as the maximum stress during the tests, together with the elongation at fracture (ε_{max}).

3. Results and discussion

3.1. Powder characterization and effect of sieving

Fig. 3 shows the FE-SEM micrographs of the Al-2618 + TiB_2 powder feedstocks obtained with the functionalization strategies implemented in this work. For all the ex-situ methods (LEM, HEM, and LPC powder samples), TiB_2 particles are observed to be attached to the surface of Al-2618 particles and homogeneously dispersed. Moreover, the functionalized powder particles maintain their spherical morphology, thus demonstrating that the different coating methods do not change the shape of the metal particles. However, it is possible to notice that in LEM feedstock, some reinforcement particles are dispersed in the powder batch without adhering to the surface of Al particles (Fig. 3.c). This phenomenon can be attributed to two main factors. First, the TiB_2 particle size used in LEM (4 μm) is larger than that used in HEM and LPC (2 μm). Smaller particles exhibit a higher tendency to adhere to surfaces due to the contribution of increased surface-area-to-volume ratio, which enhances adhesion forces such as van der Waals and electrostatic (Coulomb) interactions [36]. Second, the mechanical impact energy in LEM is lower than in HEM, which reduces the energy available to promote the effective attachment of reinforcement particles to the aluminium surface [37]. In HEM, higher impact energy facilitates stronger interfacial interactions, improving the adhesion of TiB_2 to the Al-2618 particles. Conversely, in LEM, the lower impact forces may be insufficient, leading to the presence of dispersed reinforcement particles in the powder batch. Fig. 3.g shows the cross section of a PGA powder particle, showing small TiB_2 particles (<1 μm) dispersed in the Al matrix.

All the ex-situ methods (LEM, HEM, and LPC) met the 7 wt% target of TiB_2 particles. In contrast, the pre-alloyed batch reached a maximum of approximately 2.6 wt% of TiB_2. This limitation is well known for the pre-alloying approach, and it represents one of the main reasons why ex-situ powder functionalization techniques are essential for achieving higher reinforcement contents. Increasing the TiB_2 content beyond this limit is significantly more challenging for the pre-alloyed feedstock than for ex-situ methods, where the composition can be easily adjusted by adding more borides during the mixing process. Indeed, it has been reported that the key issue in gas atomized powders with high boron content is the high reactivity of B with Ti, leading to the early formation of borides in the molten bath [38,39]. These borides are prone to separate from the liquid phase, which may not only result in a non-homogeneous distribution of borides in the final product but also in nozzle clogging during the powder production process. The addition of higher amount of boron in the pre-alloyed powder may require more complex methods, such as mixed-salt reaction methods [40], which were not employed in this study. Another promising approach could be the combination of pre-alloying with ex-situ powder functionalization. However, further studies on ex-situ functionalization methods are required to optimize the process parameters and ensure a strong and stable adhesion of the reinforcing particles to the matrix powder particles.

To assess the effect of sieving on the detachment of ceramic particles, powder samples were collected and analysed both before and after sieving with a 63 μm mesh. This evaluation aims to determine whether the sieving process influences the adhesion of TiB_2 particles to the Al

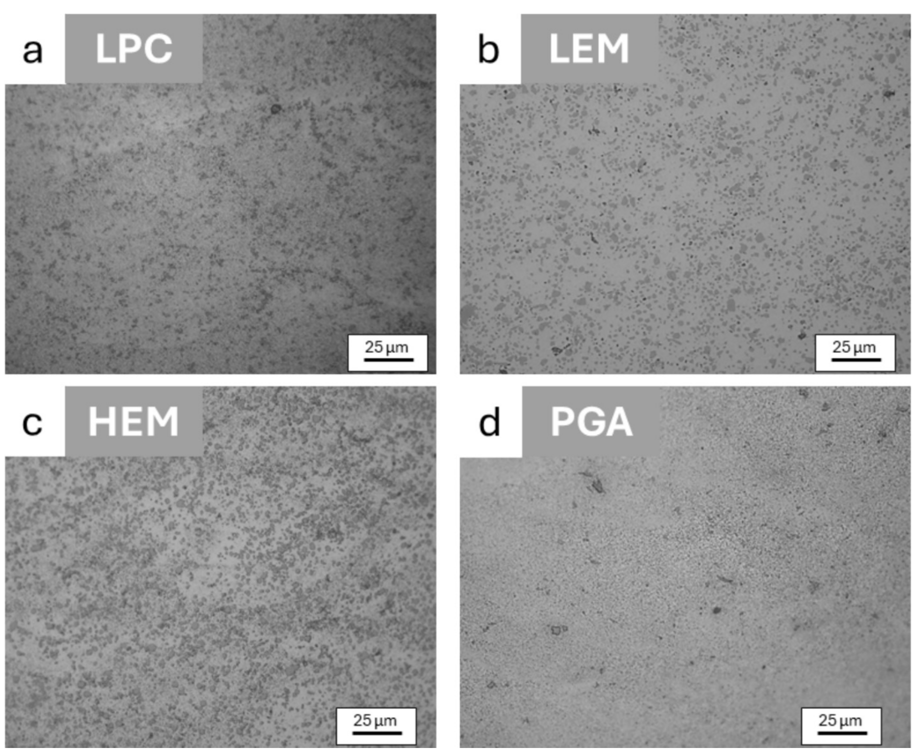

Fig. 4. LOM images of the cross-sections of the samples produced with the different powder feedstocks: a) LPC, b) LEM, c) HEM, and d) PGA.

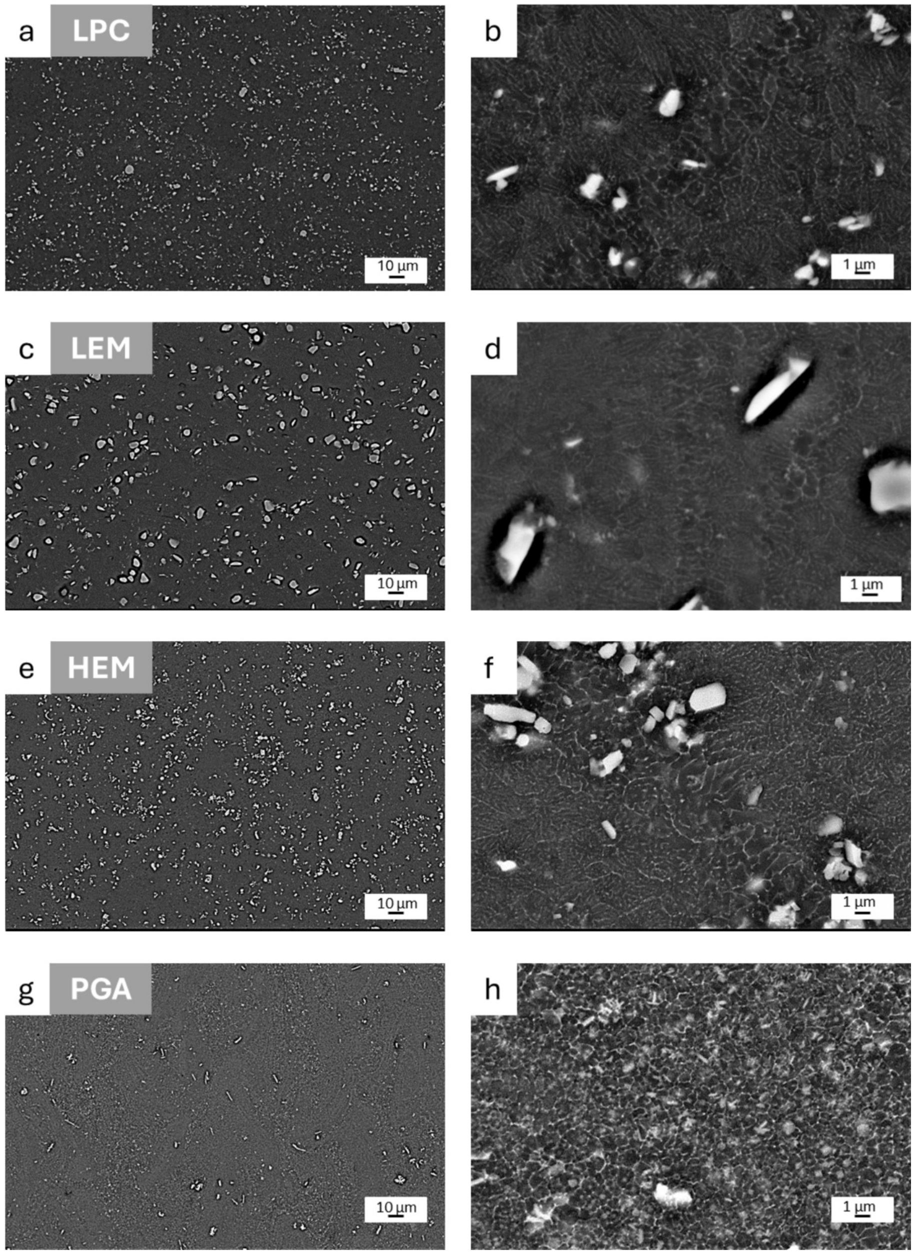

Fig. 5. FE-SEM images of the cross-sections of the samples produced with the different powder feedstocks: different powder feedstocks: a), b) LPC, c),d) LEM, e),f) HEM, and g),h) PGA.

powder particles. Understanding this effect could provide valuable insights into the reusability of the powders after sieving, specifically, it can help determine whether the powders can be reused as-is or if they require re-functionalization to restore their initial reinforcement distribution. The comparison of the FE-SEM images of the sieved and unsieved powder is also shown in Fig. 3. Quantitative analysis of TiB_2 particles was performed by ImageJ software on three FE-SEM images, these results are reported in Table 3. In LEM samples TiB_2 particles are precariously attached to the Al particles surface and the vibrations of sieving lead to the detachment and sedimentation. On the other hand, Table 3 and Fig. 3 show that sieving process does not significantly impact the amount of reinforcements attached to the powder surface for the LPC and HEM feedstocks. These results suggest that these methods enhance the adhesion of TiB_2 particles to the surface of the Al-2618 powder particles. Consequently, these powders can potentially be reused for LPBF without requiring reprocessing to improve powder homogeneity. However, it is worth mentioning that the results achieved are preliminary, and careful monitoring of the powder feedstock should be performed after each printing process to ensure a homogeneous distribution of the reinforcing particles. Additionally, it is important to study how many times the powder can be reused before any alteration in the reinforcement content occurs.

Conversely, the LEM relies on low-energy collisions between TiB_2 and Al particles, therefore the feedstock suffered from a strong reduction in borides content because of the weaker adhesion of the reinforcement phase compared to LPC and HEM. TiB_2 particles result more susceptible to detachment when exposed to external forces. Moreover, as previously stated, some TiB_2 particles in the LEM feedstock were found initially dispersed in the powder batch without adhering to the Al particle surfaces (Fig. 3.c). These unattached TiB_2 particles could sediment either during sieving or even during the printing process due to their tendency to adhere to surfaces of the Al powder. This suggests that LEM feedstocks should be re-mixed after sieving to restore a homogeneous dispersion of the reinforcement phase.

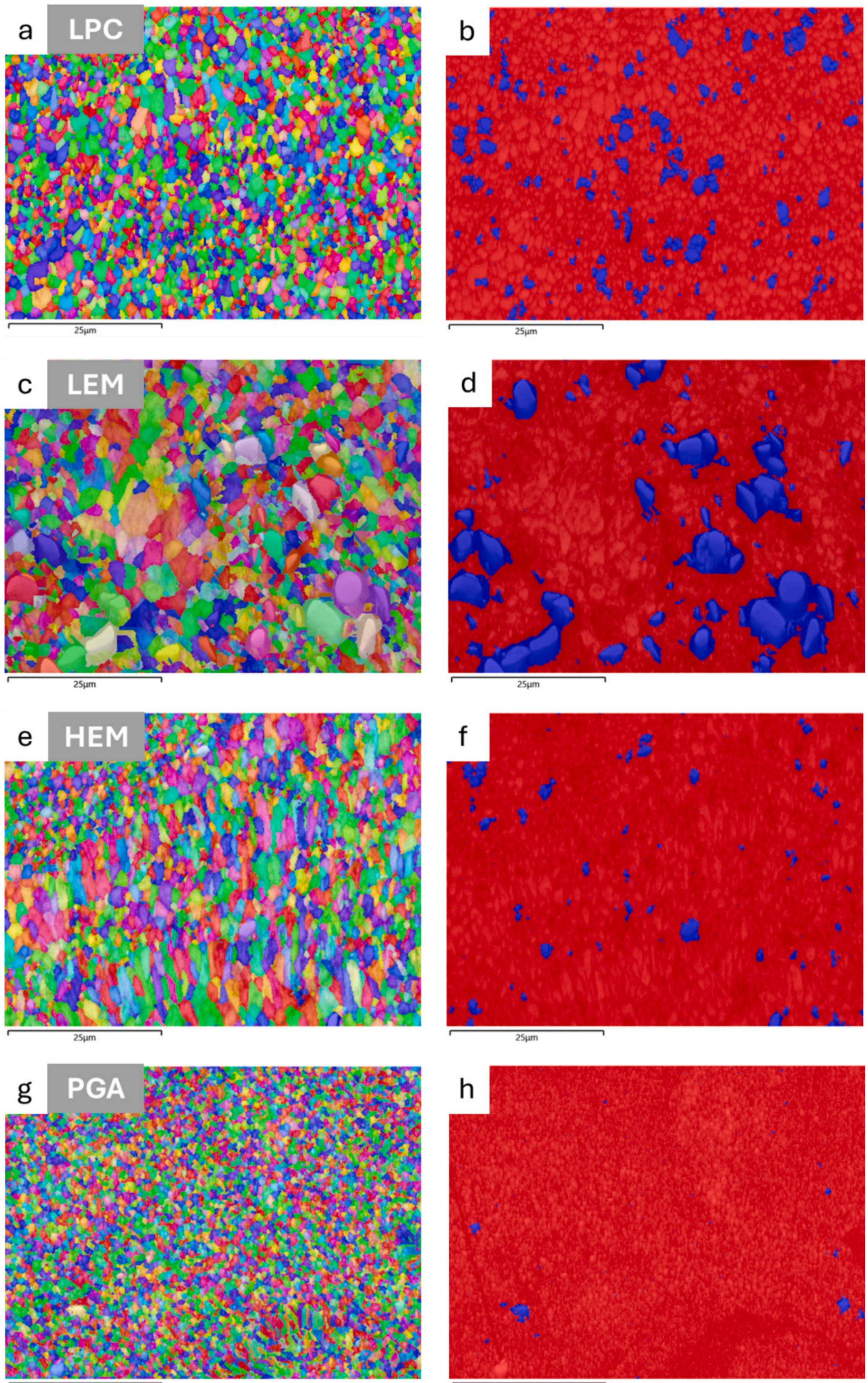

Fig. 6. EBSD results (IPFz maps and phase maps) of the cross-sections of the samples produced with the different powder feedstocks: a), b) LPC, c), d) LEM, e),f) HEM, and g),h) PGA. In the phase maps the aluminium matrix is red, TiB_2 particles are blue. (For interpretation of the references to colour in this figure legend, the reader is referred to the web version of this article.)

Table 4
Average dimensions of the grains obtained from EBSD maps.

	LPC	LEM	HEM	PGA
Average area (μm^2)	1.1	2.3	1.6	0.6
Average diameter (μm)	1.1	1.5	1.3	0.8

3.2. Characterization of as-built composites

All the powder feedstocks guaranteed sufficient flowability, which produced a proper powder bed in the form of thin layers of 25 μm. Cubic samples were successfully printed with all the powder feedstocks. The cross sections of the printed samples were analysed with LOM and FE-SEM (Fig. 4 and Fig. 5). Image analysis was conducted to estimate the porosity percentage of the printed samples, and they were found nearly

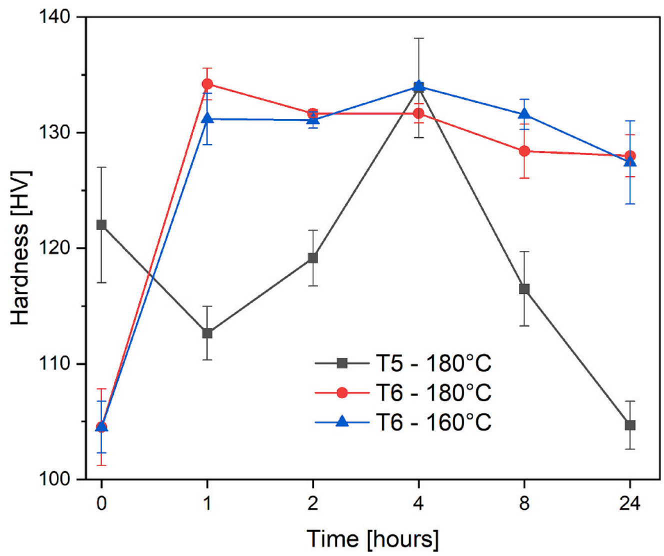

Fig. 7. Age hardening curves for samples produced from HEM powder feedstock at varying aging times.

fully dense with all the different powder feedstocks. In fact, bulk samples produced with LEM, HEM, LPC, and PAG achieved density values of 99.2 %, 99.4 %, 99.9 %, and 99.7 %, respectively. The Archimedes method confirmed the high densification levels, with measured relative density values of 99.2 %, 99.5 %, 99.4 %, and 99.1 % for the LEM, HEM, LPC, and PAG samples, respectively.

The presence of TiB_2 particles played a significant role in preventing the formation of hot cracks, a common issue in LPBF-printed Al-2618 samples [28,41]. Generally, high-strength Al alloys are particularly susceptible to hot cracking due to their large solidification interval and the presence of alloying elements such as Mg and Cu. Hot cracking occurs during solidification when the solid–liquid interface becomes unstable, leading to dendritic or cellular grain growth. As the temperature and liquid volume fraction decrease, volumetric solidification shrinkage and thermal contraction in these regions create cavities and hot cracks, which can potentially span multiple layers [42,43]. The addition of heterogeneous nucleation sites, such as inoculating phases with low undercooling, plays a crucial role in promoting nucleation at the solid–liquid interface. Grain refiners facilitate this process by inducing heterogeneous nucleation within the constitutional supercooling region at the front of the solid–liquid interface. It has been shown that both in-situ and ex-situ added particles, like TiB_2, can serve as effective heterogeneous nucleation sites [44–46].

In addition, FE-SEM and LOM images show that a uniform dispersion of the reinforcement particles was achieved with all the powder feedstocks. A uniform distribution of TiB_2 in the bulk material is crucial to produce a final product with improved and isotropic mechanical properties. This is not surprising for the PGA in-situ method, as it has been well documented in the literature that in-situ processes can lead to a good dispersion of reinforcement particles within the matrix [27,47]. However, it is interesting to note that the same uniform dispersion was also achieved with the ex-situ functionalized powders. This suggests that the TiB_2 particles are effectively and uniformly distributed on the surface of the powder particles, indicating that the various functionalization methods employed in this study (LEM, HEM, and LPC) were successful in promoting effective dispersion.

It is also worth mentioning that the amount of TiB_2 particles in the LEM, HEM, and LPC feedstocks is approximately 7 wt%, as previously stated, since these ex-situ methods allow for precise control over the reinforcement content by adjusting the amount of TiB_2 added during processing. In contrast, for the PGA feedstock, only 2.6 wt% TiB_2 was achieved. In the cross-sections of the printed PGA samples (Fig. 5.g) the TiB_2 fraction appears to be even lower. This because the reinforcement phase in this case is formed in-situ and tends to have a much finer size distribution compared to those introduced ex-situ, often reaching below 100 nm dimensions thus beyond the detection capability of FE-SEM [48].

EBSD maps were used to study the grain structure of the bulk samples, focusing on grain size and orientation. The results are presented in Fig. 6, which includes IPF maps of the different bulk materials and phase maps overlaid on Band Contrast (BC) images to highlight the TiB_2 particles (marked in blue). In all cases, borides effectively promote the heterogeneous nucleation of α-Al phase, thereby suppressing the epitaxial growth of columnar grains from previously deposited layers [49]. Indeed, TiB_2 particles are well-known grain growth inhibitors in Al that can provide a high density of low-energy-barrier heterogeneous nucleation sites ahead of the solidification front and induce a fine equiaxed structure [50,51]. As previously mentioned, such fine equiaxed grain structures can effectively prevent crack formation, indicating that all four powder functionalization methods explored in this study enhance the LPBF processability of Al-2618.

Table 4 reports the average grain size for the different powder feedstocks, expressed in terms of average area and average diameter. The data indicate that the different powder functionalization methods lead to varying degrees of grain refinement. The main difference is between samples produced with ex-situ and in-situ functionalized powder feedstocks. Indeed, the finest grain structure was observed in the sample obtained from the PGA powder, despite this feedstock having the lowest TiB_2 content. This refinement can be attributed to a dual effect: the presence of TiB_2 particles, which act as heterogeneous nucleation sites, and the excess Ti present in the PGA powder. The latter segregates at the surface of TiB_2 particles, leading to the formation of an Al_3Ti crystalline layer. Previous studies have showed that the nucleation of α-Al required a smaller undercooling in the presence of Al_3Ti compared with TiB_2, indicating that Al_3Ti is a more potent nucleant than TiB_2 [52–55]. A clear confirmation of the higher grain refinement efficiency of in-situ formed TiB_2 and Al_3Ti is provided by the comparison with ex-situ reinforced samples, which exhibit larger average grain diameters and areas. Among the ex-situ reinforcement techniques, the LEM method resulted in the largest equiaxed grain structures. However, the grain structure in this case was not completely homogeneous, with regions of relatively coarse grains coexisting with areas of very fine grains. This suggests that the size of the TiB_2 particles plays a key role in grain refinement, as finer reinforcements (such as those used in the LPC and HEM methods) were more effective in refining the microstructure. Moreover, boride particles can also act as obstacles to the grain growth. This phenomenon can be theoretically explained by the Zener pinning model, which describes how fine reinforcement particles, such as TiB_2, pin the grain boundaries during solidification, thereby limiting grain growth and promoting grain refinement. The model is expressed by in Eq. 1, where d_m is the matrix grain diameter, d_p is the reinforcement particle diameter, v_p is the volume fraction of the reinforcement, and α is the proportionality constant [56,57].

$$d_m = \left(\frac{4\alpha d_p}{3 d v_p}\right) \tag{1}$$

According to this model, smaller reinforcement particles, such as those used in the LPC and HEM powders, are more effective at pinning the grain boundaries due to their higher surface area, resulting in a finer grain structure.

3.3. Aging behaviour

An investigation on the effect of different heat-treatment routes on the mechanical properties of the materials was carried out. Al-2618 composites showed a radically different microstructure compared to Al-2618 produced by plastic deformation processes. Indeed, LPBF alloys

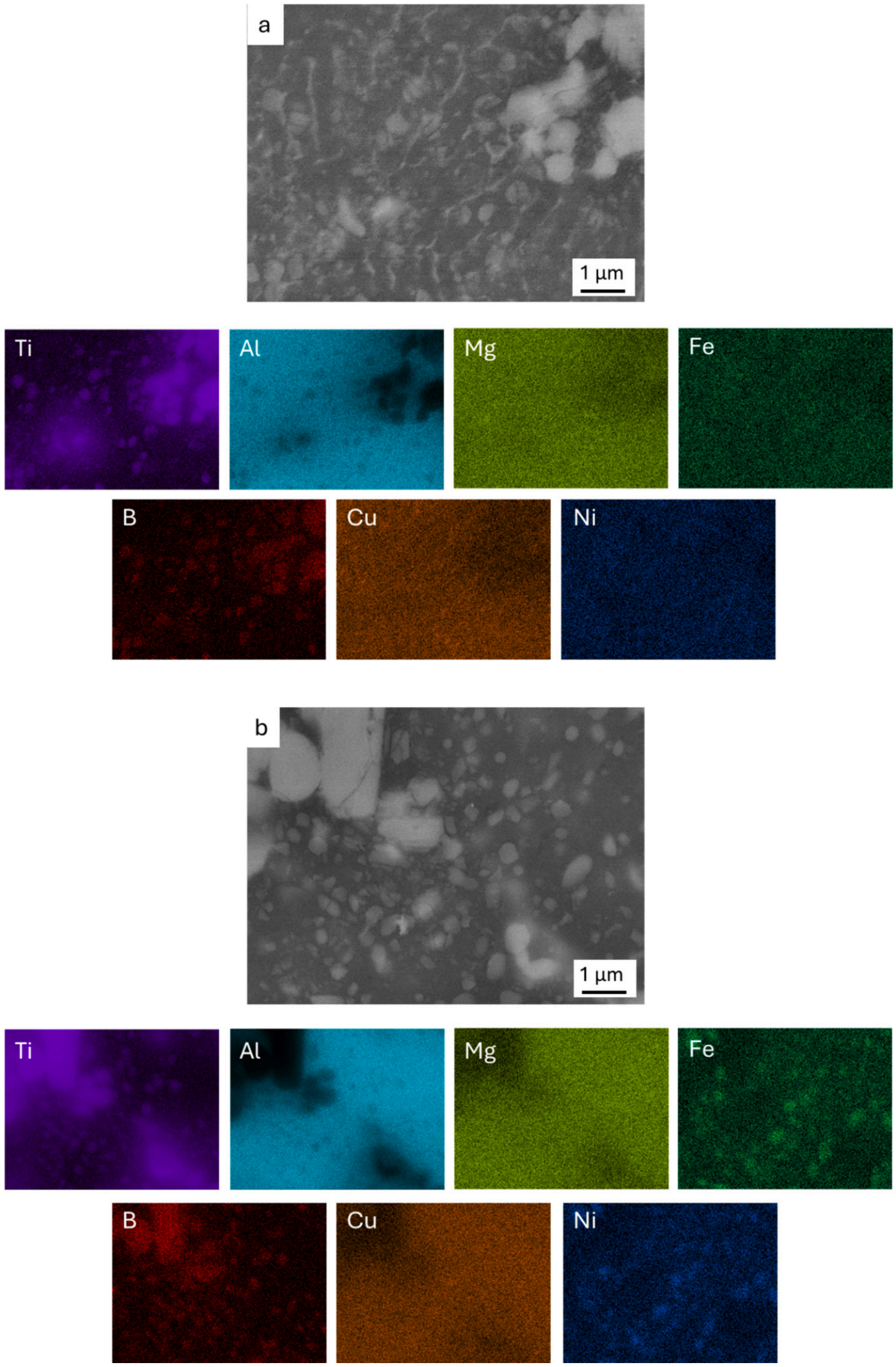

Fig. 8. FE-SEM micrographs and EDS maps of bulk material produced with HEM powder in a) T5 and b) T6–180 °C for 1 h heat-treated conditions.

show finer grain structure, smaller second phases and a supersaturated solid solution that can be exploited for direct aging treatments (T5 temper) [58–60]. Fig. 7 shows the aging time-dependency of hardness for the Al-2618/TiB_2 alloy specimens produced with HEM powder. Three different heat-treatment routes were analysed: ST at 530 °C for 1 h followed by water quenching and aging at 160 °C (T6–160 °C), solution treatment at 530 °C for 1 h followed by water quenching and aging at 180 °C (T6–180 °C), and direct aging at 180 °C (T5–180 °C).

In the AB condition, without heat treatment, the hardness was 122 ± 5 HV (point 0 h on the T5 curve), which is higher than the average hardness of an Al-2618 alloy in the as-built condition (104.0 HV). This indicates that the presence of TiB_2 borides significantly increases the hardness of the material, underscoring the role of the reinforcement phase in improving the mechanical properties of the alloy. After the solution treatment at 530 °C (point at 0 h of the T6–180 °C and T6–160 °C curves), the hardness dropped to 105 ± 3 HV. The hardness peak, corresponding to 133 ± 1 HV, was measured after aging the ST + WQ alloy at 160 °C for 4 h. Due to accelerated precipitation kinetics, the hardness peaks of the solution-treated material are shifted towards shorter aging times when the treatment is performed at higher temperatures: at 180 °C the peak hardness is reached after 1 h (134 ± 1 HV). A hardness value of 134 ± 4 HV was measured after a T5 treatment performed at 180 °C for 4 h, demonstrating that direct aging is also an effective method for increasing material hardness. Therefore, the selected treatments for mechanical testing were: ST + 180 °C for 1 h (T6), chosen for its shorter processing time, and DA 180 °C for 4 h (T5).

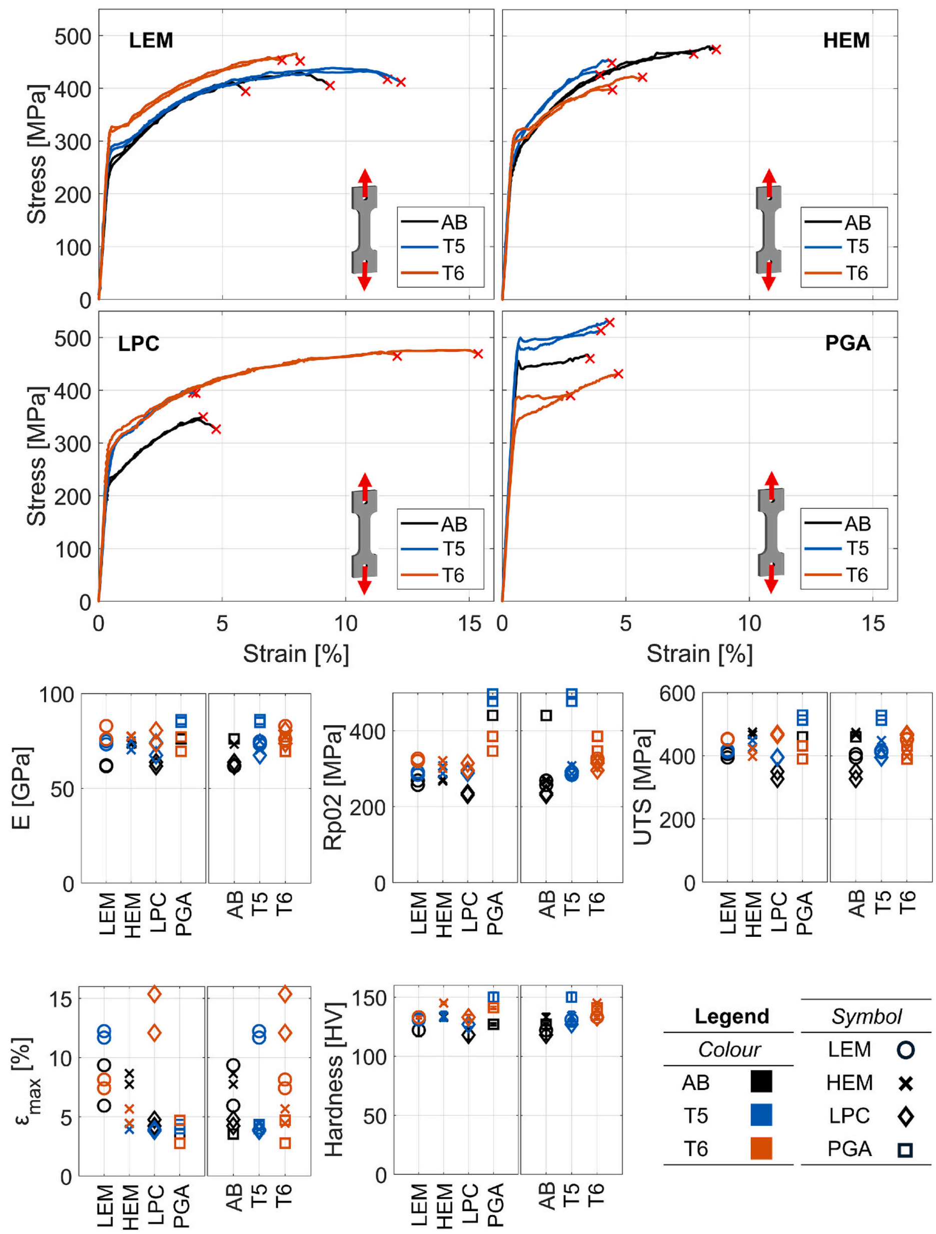

Fig. 9. Stress-strain curves of bulk materials produced with different powder feedstocks, with comparisons of mechanical properties across powders and heat treatments.

It is worth noting that the heat treatment study was conducted exclusively on samples produced with the HEM powder feedstock. However, variations in TiB_2 particle size and distribution across the different powders could influence aging behaviour. To maintain consistency and enable a direct comparison between the different materials, the same heat treatment cycles were applied to all samples, regardless of feedstock.

The microstructure of the selected samples was analysed with FE-SEM, with the results shown in Fig. 8. In the T5 condition, the material retains the cellular structure present in the as-built condition. Micro-segregations at the cell boundaries are very thin, making their composition difficult to be measured by FE-SEM-EDS. A previous study on Al-2618 indicated that higher weight fractions of Cu, Fe, and Ni are typically found at the cell boundaries [59]. T6 heat treatment significantly changes the as-built microstructure, resulting in the formation of spherical precipitates. Elemental composition maps obtained by EDS (Fig. 8) reveal that these precipitates are rich in Ni and Fe, so they could be ascribed to Al_9FeNi particles [28].

3.4. Tensile properties

All the tensile curves are reported in Fig. 9. For each feedstock powder, two curves are presented for each heat treatment condition. The black lines describe the AB condition, the blue lines represent the T5 condition and the red lines the T6 (ST+ aging 180 °C for 1 h) condition. Good repeatability is clearly observable among the couple of curves of each condition. The obtained mechanical properties are reported in Fig. 9. The same dataset of each property was grouped by powder (left side of the plot) and by heat treatment (right side of the plot) to obtain an easier comparison and identification of possible trends.

It is worth mentioning that the adopted sample geometry is representative of a thin wall structure having a thickness under 1 mm in its final shape. However, the reduced cross section significantly increases the influence of defects on the mechanical performance. Therefore, the achieved results are suitable for obtaining preliminary insights into the material properties. These results should be considered a lower bound for the theoretical properties of a bulk standard sample.

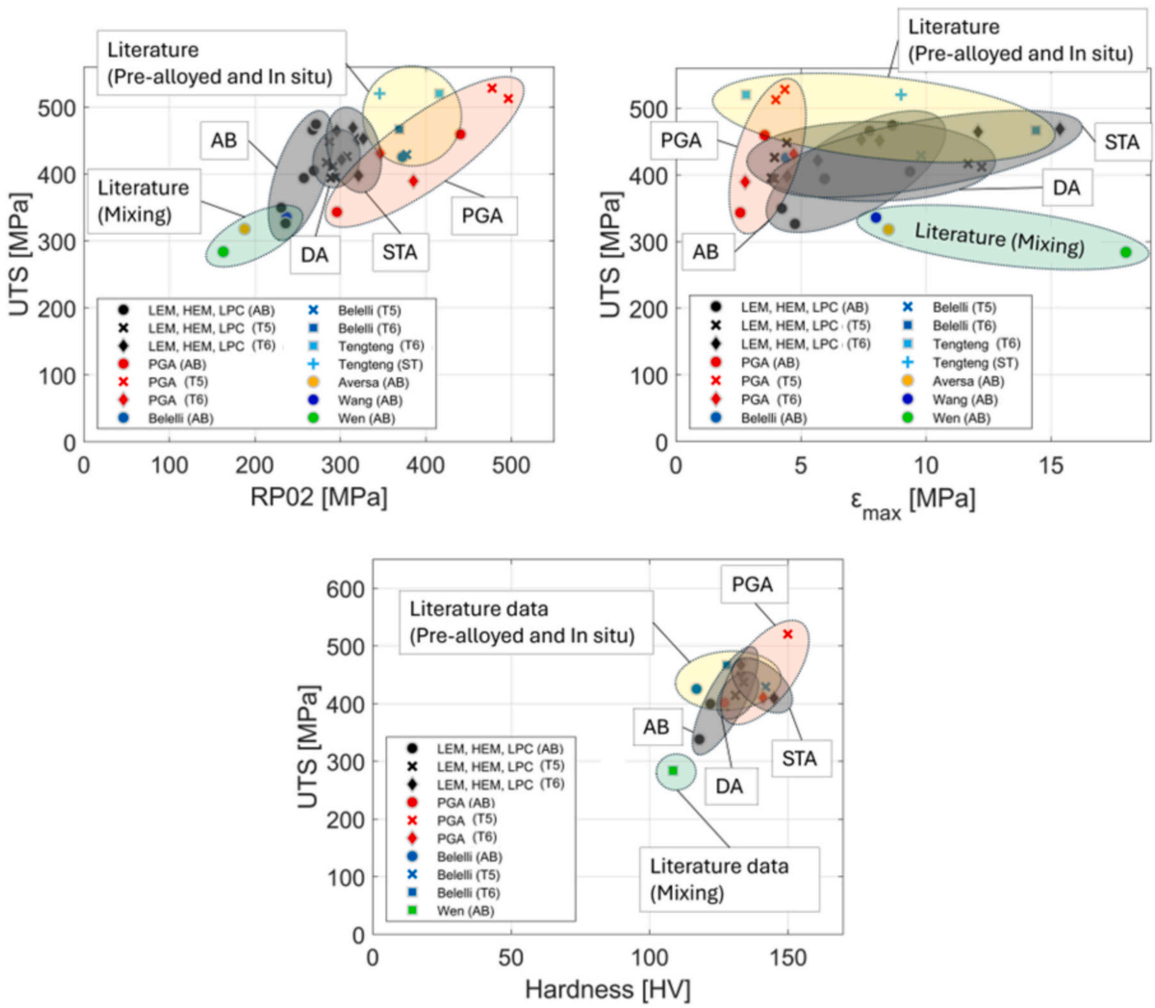

Fig. 10. Ashby maps showing UTS vs. Rp0.2, UTS vs. εmax, and UTS vs. hardness for different MMC produced with different powder feedstocks.

Table 5
Information regarding the powder feedstocks used in the literature works reported in Fig. 10.

Author	Al matrix	Method	Particles size	Ref.
Belelli	Al-2618	Pre-alloyed	nm	[28]
Tengteng	AlCuMg	In situ	nm	[65]
Aversa	AlSi10Mg	Mech. Mixing	2–5 μm	[64]
Wang	2024	Mech. Mixing	nm	[66]
Wen	2024	Mech. Mixing	nm	[67]

There is a detectable increasing trend in Rp02 and UTS as a function of the heat treatment. In fact, both T5 and T6 seem to increase the yield and ultimate strengths. The same trend can be noticed for the elastic modulus. On the other hand, the data are consistent among the different powders. Regarding the elongation at fracture, the large scatter of the data is evident. This is closely related to the thin wall shape, which significantly increases the influence of defects on the sample rupture. Nevertheless, high elongations were reached in particular for materials produced with LEM and LPC powders in T6 condition where values exceeding 10 % were observed.

A separate discussion is warranted for the samples printed with pre-alloyed powder. As highlighted in Section 3.2, pre-alloyed powder is highly effective in promoting the in-situ formation of nano-metric TiB_2, leading to further grain refinement. This results in a higher yield and ultimate strengths compared to the other three powders, though at the expense of the ductility. Both Rp02 and UTS reach 500 MPa in T5 condition, which appears to be the most effective heat treatment for the bulk material produced with the pre-alloyed powder. This observation is also confirmed by the hardness measurements on the tested samples. Conversely, the T6 heat treatment results in a decrease in mechanical performance. The higher strength of the samples produced with PGA powder feedstock can be explained by different well known strengthening mechanisms, such as load transfer, Hall–Petch (i.e., grain refinement), Orowan, coefficients of thermal expansion (CTE), and/or elastic modulus (EM) mismatch strengthening [61,62]. Among these, the Hall–Petch mechanism plays a dominant role in enhancing the material's strength, as it is directly influenced by the grain size of the final microstructure [56,63]. The in-situ formation of nanometric TiB_2 particles in the PGA alloy leads to a significantly finer grain structure compared to ex-situ reinforced materials. A smaller grain size, as observed in the PGA material, effectively increases the grain boundary density, restricting dislocation movement and thereby enhancing the Rp02 and UTS. However, while these strengthening mechanisms improve mechanical performance, particularly in terms of strength, they also lead to a reduction in ductility, toughness, and strain to failure, as commonly observed in materials with ultra-fine grain structures [62].

Fig. 10 summarises the mechanical properties obtained in this study with literature data on similar feedstock powders. Table 5 highlights the composition of the metallic powders, indicating different aluminium matrices and production methods. The matrices include 2xxx series alloys and AlSi10Mg, produced either through pre-alloying or mechanical mixing. The reinforcement particles (TiB_2) range in size from nanometers to micrometers. For instance, Belelli uses pre-alloyed powders [28], while Aversa employs mechanical mixing with micrometric TiB_2 particles [64]. Literature data displayed in Fig. 10 are divided into powders produced by mechanical mixing (green bubble) and those produced by pre-alloying and in-situ reaction (yellow bubble). Tensile data are grouped into pre-alloyed powder (red bubble) and those produced by mechanical mixing and plasma coating (grey bubbles), with subdivisions by heat treatment: AB, T5 and T6.

The first plot (UTS vs. Rp02) clearly shows that the ex-situ reinforced powder feedstocks used in this work fall below literature data for powders produced by pre-alloying and in-situ reaction, but they are positioned well above the mechanically mixed powders. In contrast, the strain at failure aligns with powders produced by pre-alloying and in-situ reaction. This can be considered a promising result considering the thin-wall shape of the specimens adopted in this study. Data collected from the pre-alloyed powder in this work show Rp_{02} and UTS reaching the same values as those reported in literature for pre-alloyed powders. However, as already observed, the ductility of this material is lower to both the other powders of this study and those reported in the literature.

Finally, regarding the hardness values, they generally fall within the same range, except for literature data on mechanical mixing which shows lower hardness. Also, pre-alloyed powder in the T5 condition (red x) is out of range: T5 has already been evaluated as the most effective heat treatment for bulk materials produced with this powder batch.

4. Concluding remarks

In this study, Al-2618-TiB_2 powder feedstocks with a high reinforcement fraction were successfully produced using powder functionalization methods including low-energy mechanical mixing, high-energy mechanical mixing, plasma coating, and pre-alloying. Ex-situ methods such as high-energy mixing and plasma coating effectively dispersed TiB_2 particles on the surfaces of Al alloy particle. In contrast, low-energy mixing showed poorer adhesion and dispersion capabilities. Regarding TiB_2 content, high fractions were achieved with ex-situ methods, while pre-alloyed batches reached approximately 2.6 wt%, highlighting the challenge of increasing B content during gas atomization.

All feedstocks were successfully printed by LPBF. Analysis using LOM and FE-SEM confirmed a homogeneous dispersion of reinforcement particles. TiB_2 particles effectively suppressed the formation of hot cracks and promoted grain refinement. Despite gas-atomized powders exhibiting significantly lower levels of Ti and B, the in-situ formation of nanometric TiB_2 particles, along with the presence of an excess of Ti, proved to be the most effective in promoting grain refinement. As a result, the material produced from the pre-alloyed powder achieved the highest strength levels compared to ex-situ reinforced powders.

CRediT authorship contribution statement

G. Lupi: Writing – original draft, Methodology, Investigation, Formal analysis, Data curation, Conceptualization. **L. Mariotti:** Writing – original draft, Methodology, Investigation, Formal analysis, Data curation, Conceptualization. **A. Mistrini:** Methodology, Formal analysis, Investigation, Data curation. **J. Larsson:** Writing – review & editing, Supervision, Project administration, Formal analysis. **L. Patriarca:** Writing – review & editing, Supervision, Resources, Methodology, Investigation, Formal analysis, Conceptualization. **R. Casati:** Conceptualization, Writing – review & editing, Supervision, Resources, Project administration, Methodology, Funding acquisition, Formal analysis.

Declaration of competing interest

The authors declare that the work has not been published previously except in the form of a preprint, an abstract, a published lecture, academic thesis or registered report.

Acknowledgements

This study was accomplished within the ENCOMPASS (Design of Enhanced Metal Matrix Composites for Additive Manufacturing of Space Structures) funded by the European Space Agency.

Data availability

The data that support the findings of this study are available on request from the corresponding author, RC.

References

[1] M.M. Francois, A. Sun, W.E. King, N.J. Henson, D. Tourret, C.A. Bronkhorst, et al., Modeling of additive manufacturing processes for metals: challenges and opportunities, Curr. Opin. Solid State Mater. Sci. 21 (2017) 198–206, https://doi.org/10.1016/J.COSSMS.2016.12.001.

[2] R. Raju, N. Manikandan, D. Palanisamy, D. Arulkirubakaran, J.S. Binoj, P. Thejasree, et al., A review of challenges and opportunities in additive manufacturing, Lect. Notes in Mechanical Engineering (2022) 23–29, https://doi.org/10.1007/978-981-19-0244-4_3/COVER.

[3] S.S. Babu, L. Love, R. Dehoff, W. Peter, T.R. Watkins, S. Pannala, Additive manufacturing of materials: opportunities and challenges, MRS Bull. 40 (2015) 1154–1161, https://doi.org/10.1557/MRS.2015.234.

[4] D. Herzog, V. Seyda, E. Wycisk, C. Emmelmann, Additive manufacturing of metals, Acta Mater. 117 (2016) 371–392, https://doi.org/10.1016/J.ACTAMAT.2016.07.019.

[5] T. DebRoy, H.L. Wei, J.S. Zuback, T. Mukherjee, J.W. Elmer, J.O. Milewski, et al., Additive manufacturing of metallic components – process, structure and properties, Prog. Mater. Sci. 92 (2018) 112–224, https://doi.org/10.1016/J.PMATSCI.2017.10.001.

[6] M.S. Kenevisi, Y. Yu, F. Lin, A review on additive manufacturing of Al–cu (2xxx) aluminium alloys, processes and defects 37 (2021) 805–829, https://doi.org/10.1080/02670836.2021.1958487.

[7] T. Fedina, F. Belelli, G. Lupi, B. Brandau, R. Casati, R. Berneth, et al., Influence of AlSi10Mg powder aging on the material degradation and its processing in laser powder bed fusion, Powder Technol. 412 (2022) 118024, https://doi.org/10.1016/J.POWTEC.2022.118024.

[8] K. Geng, Y. Yang, S. Li, R.D.K. Misra, Q. Zhu, Enabling high-performance 3D printing of Al powder by decorating with high laser absorbing co phase, Addit. Manuf. 32 (2020) 101012, https://doi.org/10.1016/J.ADDMA.2019.101012.

[9] T. Romano, M. Vedani, Additive Manufacturing of Pure Copper: Technologies and Applications. Copper - From the Mineral to the Final Application, IntechOpen, 2023, https://doi.org/10.5772/intechopen.107233.

[10] O. Hentschel, L. Siegel, C. Scheitler, F. Huber, D. Junker, A. Gorunow, et al., Processing of AISI H11 tool steel powder modified with carbon black nanoparticles for the additive manufacturing of forging tools with tailored mechanical properties by means of laser metal deposition (LMD), Metals (Basel) 8 (2018) 659, https://doi.org/10.3390/met8090659.

[11] C. Doñate-Buendia, P. Kürnsteiner, F. Stern, M.B. Wilms, R. Streubel, I.M. Kusoglu, et al., Microstructure formation and mechanical properties of ODS steels built by laser additive manufacturing of nanoparticle coated iron-chromium powders, Acta Mater. (2021) 206, https://doi.org/10.1016/J.ACTAMAT.2020.116566.

[12] B.M. Arkhurst, J.J. Park, C.H. Lee, J.H. Kim, Direct laser deposition of 14Cr oxide dispersion strengthened steel powders using Y_2O_3 and HfO_2 Dispersoids, Korean J. Metals Mater. 55 (2017) 550–558, https://doi.org/10.3365/KJMM.2017.55.8.550.

[13] S. Dadbakhsh, L. Hao, P.G.E. Jerrard, D.Z. Zhang, Experimental investigation on selective laser melting behaviour and processing windows of in situ reacted Al/Fe 2O 3 powder mixture, Powder Technol. 231 (2012) 112–121, https://doi.org/10.1016/J.POWTEC.2012.07.061.

[14] S. Dadbakhsh, L. Hao, Effect of Al alloys on selective laser melting behaviour and microstructure of in situ formed particle reinforced composites, J. Alloys Compd. 541 (2012) 328–334, https://doi.org/10.1016/J.JALLCOM.2012.06.097.

[15] K.J. Lijay, J.D.R. Selvam, I. Dinaharan, S.J. Vijay, Microstructure and mechanical properties characterization of AA6061/TiC aluminum matrix composites synthesized by in situ reaction of silicon carbide and potassium fluotitanate, Trans. Nonferr. Metals Soc. China (English Edition) 26 (2016) 1791–1800, https://doi.org/10.1016/S1003-6326(16)64255-3.

[16] A. Martín, C.M. Cepeda-Jiménez, M.T. Pérez-Prado, Gas atomization of γ-TiAl alloy powder for additive manufacturing, Adv. Eng. Mater. (2020) 22, https://doi.org/10.1002/ADEM.201900594.

[17] A. Lawley, Atomization of specialty alloy powders, J. Metals 33 (1981) 13–18, https://doi.org/10.1007/BF03354395/METRICS.

[18] Katz-Demyanetz A, Koptyug A, Popov V V. In-situ Alloying as a Novel Methodology in Additive Manufacturing. Proceedings of the 2020 IEEE 10th international conference on "nanomaterials: applications and properties", NAP 2020 2020. doi: https://doi.org/10.1109/NAP51477.2020.9309652.

[19] U.A. Essien, S. Vaudreuil, In-situ metal matrix composites development for additive manufacturing: a perspective, J. Achiev. Mater. Manufact. Eng. 111 (2022) 78–85, https://doi.org/10.5604/01.3001.0015.9997.

[20] D. Gu, Z. Wang, Y. Shen, Q. Li, Y. Li, In-situ TiC particle reinforced Ti-Al matrix composites: powder preparation by mechanical alloying and selective laser melting

behavior, Appl. Surf. Sci. 255 (2009) 9230–9240, https://doi.org/10.1016/J.APSUSC.2009.07.008.
[21] A. Mussatto, I.U.I. Ahad, R.T. Mousavian, Y. Delaure, D. Brabazon, Advanced production routes for metal matrix composites, Eng. Rep. 3 (2021) e12330, https://doi.org/10.1002/ENG2.12330.
[22] R. Bidulsky, F.S. Gobber, J. Bidulska, M. Ceroni, T. Kvackaj, M.A. Grande, Coated Metal Powders for Laser Powder Bed Fusion (L-PBF) Processing: A Review, Metals 11 (2021) 1831, https://doi.org/10.3390/MET11111831.
[23] E. Fereiduni, A. Ghasemi, M. Elbestawi, Selective laser melting of hybrid ex-situ/in-situ reinforced titanium matrix composites: laser/powder interaction, reinforcement formation mechanism, and non-equilibrium microstructural evolutions, Mater. Des. 184 (2019) 108185, https://doi.org/10.1016/J.MATDES.2019.108185.
[24] S. Dadbakhsh, R. Mertens, L. Hao, J. Van Humbeeck, J.P. Kruth, Selective laser melting to manufacture "in situ" metal matrix composites: A review, Adv. Eng. Mater. 21 (2019) 1801244, https://doi.org/10.1002/ADEM.201801244.
[25] Y. Liu, S. Li, R.D.K. Misra, K. Geng, Y. Yang, Planting carbon nanotubes within Ti-6Al-4V to make high-quality composite powders for 3D printing high-performance Ti-6Al-4V matrix composites, Scr. Mater. 183 (2020) 6–11, https://doi.org/10.1016/J.SCRIPTAMAT.2020.03.009.
[26] F. Belelli, R. Casati, M. Riccio, A. Rizzi, M.Y. Kayacan, M. Vedani, Development of a novel high-temperature al alloy for laser powder bed fusion, Metals (Basel) 11 (2021) 1–12, https://doi.org/10.3390/MET11010035.
[27] F. Belelli, R. Casati, M. Vedani, Development of Al-cu-mg and Al-mg-Si-Zr alloys with improved L-PBF Processability, Mineral. Met. Mater. Series (2022) 289–297, https://doi.org/10.1007/978-3-030-92381-5_26.
[28] F. Belelli, R. Casati, F. Larini, M. Riccio, M. Vedani, Investigation on two Ti–B-reinforced Al alloys for laser powder bed fusion, Mater. Sci. Eng. A 808 (2021) 140944, https://doi.org/10.1016/J.MSEA.2021.140944.
[29] K.U. Kainer, Metal Matrix Composites: Custom-Made Materials for Automotive and Aerospace Engineering, John Wiley and Sons, 2006 doi:10.1002/3527608117; CSUBTYPE:STRING:EDITED.
[30] Kymera International. https://www.kymerainternational.com/, 2025.
[31] IMR Metalle GmbH. https://www.imr-metalle.com/en/products/metal-powders, 2025.
[32] A.B. Höganäs. https://www.hoganas.com/, 2025.
[33] Treibacher industrie AG. https://treibacher.com/en/, 2025.
[34] AM4AM s.à.r.l. https://www.am-4-am.com/, 2025 (accessed April 29, 2025).
[35] ImageJ. https://imagej.net/ij/, 2025 (accessed April 29, 2025).
[36] W. Zhai, W. Zhou, S.M.L. Nai, J. Wei, Characterization of nanoparticle mixed 316L powder for additive manufacturing, J. Mater. Sci. Technol. 47 (2020) 162–168, https://doi.org/10.1016/J.JMST.2020.02.019.
[37] J. Long, C. Wang, J. Zhu, X. Zhan, Z. Sun, B. Shen, et al., Discrete element simulation for mixing performances and power consumption in a twin-blade planetary mixer with non-cohesive particles, Adv. Powder Technol. 33 (2022) 103437, https://doi.org/10.1016/J.APT.2022.103437.
[38] A. Ünal, Production of rapidly solidified Aluminium alloy powders by gas atomisation and their applications, Powder Metall. 33 (1990) 53–64, https://doi.org/10.1179/POM.1990.33.1.53.
[39] L. Lu, M.O. Lai, H.Y. Wang, Synthesis of titanium diboride TiB2 and Ti-Al-B metal matrix composites, J. Mater. Sci. 35 (2000) 241–248, https://doi.org/10.1023/A:1004789910279/METRICS.
[40] J. Kellie, J. Wood, Reaction processing in the metals industry, Materials World 3 (1995) 10–12.
[41] H. Zhang, H. Zhu, X. Nie, J. Yin, Z. Hu, X. Zeng, Effect of zirconium addition on crack, microstructure and mechanical behavior of selective laser melted Al-cu-mg alloy, Scr. Mater. 134 (2017) 6–10, https://doi.org/10.1016/J.SCRIPTAMAT.2017.02.036.
[42] M. Schuster, A. De Luca, R. Widmer, X. Maeder, C. Leinenbach, Processability, microstructure and precipitation of a Zr-modified 2618 aluminium alloy fabricated by laser powder bed fusion, J. Alloys Compd. 913 (2022) 165346, https://doi.org/10.1016/J.JALLCOM.2022.165346.
[43] J.H. Martin, D. Yahata, J.M. Hundley, J.A. Mayer, T.A. Schaedler, T.M. Pollock, 3D printing of high-strength aluminium alloys, Nature 549 (2017) 365–369, https://doi.org/10.1038/nature23894.
[44] M.X. Zhang, P.M. Kelly, M.A. Easton, J.A. Taylor, Crystallographic study of grain refinement in aluminum alloys using the edge-to-edge matching model, Acta Mater. 53 (2005) 1427–1438, https://doi.org/10.1016/J.ACTAMAT.2004.11.037.
[45] X. Li, G. Li, M.X. Zhang, Q. Zhu, Novel approach to additively manufacture high-strength Al alloys by laser powder bed fusion through addition of hybrid grain refiners, Addit. Manuf. 48 (2021) 102400, https://doi.org/10.1016/J.ADDMA.2021.102400.
[46] A. Durga, N.H. Pettersson, S.B.A. Malladi, Z. Chen, S. Guo, L. Nyborg, et al., Grain refinement in additively manufactured ferritic stainless steel by in situ inoculation using pre-alloyed powder, Scr. Mater. 194 (2021) 113690, https://doi.org/10.1016/J.SCRIPTAMAT.2020.113690.
[47] F. Belelli, R. Casati, M. Vedani, J. Volpp, Design and characterization of Al–mg–Si–Zr alloys with improved laser powder bed fusion Processability, Metall. Mater. Trans. A 53 (2021) 331–343, https://doi.org/10.1007/S11661-021-06531-Y.
[48] S. Feng, S. Guan, S. Zhang, S. Mooraj, M. Luebbe, X. Fan, et al., Ultrafine-grained Fe-TiB2 high-modulus nanocomposite steel with high strength and isotropic mechanical properties by laser powder bed fusion, Addit. Manuf. 70 (2023) 103569, https://doi.org/10.1016/j.addma.2023.103569.
[49] G.K. Sigworth, T.A. Kuhn, Grain refinement of aluminum casting alloys, Int. J. Metalcasting/Fall (7) (2007).
[50] X.P. Li, G. Ji, Z. Chen, A. Addad, Y. Wu, H.W. Wang, et al., Selective laser melting of nano-TiB2 decorated AlSi10Mg alloy with high fracture strength and ductility, Acta Mater. 129 (2017) 183–193, https://doi.org/10.1016/J.ACTAMAT.2017.02.062.
[51] X. Wen, Q. Wang, Q. Mu, N. Kang, S. Sui, H. Yang, et al., Laser solid forming additive manufacturing TiB2 reinforced 2024Al composite: microstructure and mechanical properties, Mater. Sci. Eng. A 745 (2019) 319–325, https://doi.org/10.1016/J.MSEA.2018.12.072.
[52] Z. Fan, Y. Wang, Y. Zhang, T. Qin, X.R. Zhou, G.E. Thompson, et al., Grain refining mechanism in the Al/Al–Ti–B system, Acta Mater. 84 (2015) 292–304, https://doi.org/10.1016/J.ACTAMAT.2014.10.055.
[53] N. Iqbal, N.H. van Dijk, T. Hansen, L. Katgerman, G.J. Kearley, The role of solute titanium and TiB2 particles in the liquid–solid phase transformation of aluminum alloys, Mater. Sci. Eng. A 386 (2004) 20–26, https://doi.org/10.1016/J.MSEA.2004.06.068.
[54] J. Li, F.S. Hage, Q.M. Ramasse, P. Schumacher, The nucleation sequence of α-Al on TiB2 particles in Al-cu alloys, Acta Mater. 206 (2021) 116652, https://doi.org/10.1016/J.ACTAMAT.2021.116652.
[55] N. Iqbal, N.H. van Dijk, S.E. Offerman, N. Geerlofs, M.P. Moret, L. Katgerman, et al., In situ investigation of the crystallization kinetics and the mechanism of grain refinement in aluminum alloys, Mater. Sci. Eng. A 416 (2006) 18–32, https://doi.org/10.1016/J.MSEA.2005.10.045.
[56] A. Sanaty-Zadeh, Comparison between current models for the strength of particulate-reinforced metal matrix nanocomposites with emphasis on consideration of Hall–Petch effect, Mater. Sci. Eng. A 531 (2012) 112–118, https://doi.org/10.1016/J.MSEA.2011.10.043.
[57] B. AlMangour, M.S. Baek, D. Grzesiak, K.A. Lee, Strengthening of stainless steel by titanium carbide addition and grain refinement during selective laser melting, Mater. Sci. Eng. A 712 (2018) 812–818, https://doi.org/10.1016/J.MSEA.2017.11.126.
[58] R. Casati, M. Coduri, S. Checchia, M. Vedani, Insight into the effect of different thermal treatment routes on the microstructure of AlSi7Mg produced by laser powder bed fusion, Mater. Charact. 172 (2021) 110881, https://doi.org/10.1016/J.MATCHAR.2021.110881.
[59] R. Casati, J.N. Lemke, A.Z. Alarcon, M. Vedani, Aging behavior of high-strength Al alloy 2618 produced by selective laser melting, Metall. Mater. Trans. A 48 (2017) 575–579, https://doi.org/10.1007/s11661-016-3883-y.
[60] J.T.O. de Menezes, E.M. Castrodeza, L. Patriarca, R. Casati, Effect of heat treatments and loading orientation on the tensile properties and fracture toughness of AlSi7Mg alloy produced by laser powder bed fusion, Int. J. Fract. 235 (2022) 145–157, https://doi.org/10.1007/s10704-022-00631-5.
[61] Q.Z. Wang, X. Lin, N. Kang, X.L. Wen, Y. Cao, J.L. Lu, et al., Effect of laser additive manufacturing on the microstructure and mechanical properties of TiB2 reinforced Al-cu matrix composite, Mater. Sci. Eng. A 840 (2022) 142950, https://doi.org/10.1016/J.MSEA.2022.142950.
[62] C.S. Kim, K. Cho, M.H. Manjili, M. Nezafati, Mechanical performance of particulate-reinforced Al metal-matrix composites (MMCs) and Al metal-matrix nano-composites (MMNCs), J. Mater. Sci. 52 (2017) 13319–13349, https://doi.org/10.1007/S10853-017-1378-X/METRICS.
[63] R. Casati, M. Vedani, Metal matrix composites reinforced by Nano-particles—A review, Metals (Basel) 4 (2014) 65–83, https://doi.org/10.3390/MET4010065.
[64] A. Aversa, G. Marchese, M. Lorusso, F. Calignano, S. Biamino, E.P. Ambrosio, et al., Microstructural and Mechanical Characterization of Aluminum Matrix Composites Produced by Laser Powder Bed Fusion, 2017, https://doi.org/10.1002/adem.201700180.
[65] T. Sun, J. Chen, Y. Wu, M. Wang, Y. Fu, H. Wang, et al., Achieving excellent strength of the LPBF additively manufactured Al–cu–mg composite via in-situ mixing TiB2 and solution treatment, Mater. Sci. Eng. A 850 (2022) 143531, https://doi.org/10.1016/j.msea.2022.143531.
[66] Q.Z. Wang, X. Lin, N. Kang, X.L. Wen, Y. Cao, J.L. Lu, et al., Effect of laser additive manufacturing on the microstructure and mechanical properties of TiB2 reinforced Al-cu matrix composite, Mater. Sci. Eng. A (2022) 840, https://doi.org/10.1016/j.msea.2022.142950.
[67] X. Wen, Q. Wang, Q. Mu, N. Kang, S. Sui, H. Yang, et al., Laser solid forming additive manufacturing TiB2 reinforced 2024Al composite: microstructure and mechanical properties, Mater. Sci. Eng. A 745 (2019) 319–325, https://doi.org/10.1016/j.msea.2018.12.072.